Egypt. J. Chem. **Vol. 67**, No. 4 pp. 411 - 422 (2024)

Egyptian Journal of Chemistry

http://ejchem.journals.ekb.eg/

Production of polyvinyl alcohol/natural hydroxyapatite/magnesia/silicon carbide hybrid composites for use in orthopedic applications: Optical, electrical, and mechanical properties

Dalia E. Abulyazied1,2*, Asma M. Alturki3, Ayshah S. Alatawi1, R. Bousbih1, R Alamlah1, H. M. Abomostafa4, G. M. El komy5, Mohammed A. Taha6, 7, Rasha A. Youness8, *

[1]*Physics Department, Faculty of Science, University of Tabuk, Tabuk, Saudi Arabia*
[2]*Department of Petrochemical, Egyptian Petroleum Research Institute (EPRI), Nasr City, Cairo, Egypt*
[3]*Chemistry Department, Faculty of Science, University of Tabuk, Tabuk, Saudi Arabia*
[4]*Physics Department, Faculty of Science, Menoufia University, Shebin Elkom, Egypt*
[5] *Electron Microscope and Thin Film Department, National Research Center, Dokki, Giza 12622, Egypt*
[6]*Solid State Physics Department, National Research Centre, El Buhouth St., 12622 Dokki, Giza, Egypt*
[7]*Pharos University in Alexandria, Smoha, Egypt*
[8]*Spectroscopy Department, National Research Centre, El Buhouth St., 12622 Dokki, Giza, Egypt*

Abstract

Biopolymers are promising materials that could be widely used in bone replacement applications if both their low mechanical and bioactivity properties are improved. In this regard, the main objective of this study was to improve the mechanical and biological properties in addition to improving the optical and electrical properties to be suitable for use in fracture healing purposes. Therefore, in this study, a batch of poly(vinyl alcohol; PVA) and biologically extracted hydroxyapatite (BHA) was mechanically blended in a ratio of (70:30 vol.%). Then, magnesium oxide (MgO) and silicon carbide (SiC) were added to this batch with different volume percentages and hot-pressed at 120 °C. The physical, mechanical, optical and electrical properties were measured. Additionally, the ability of these samples to form an apatite layer on their surfaces was evaluated by soaking them in simulated body fluid (SBF) and then examined by scanning electron microscopy (SEM). The results obtained clarified that the mechanical properties in terms of microhardness, compressive strength, Young's modulus, longitudinal modulus, bulk modulus, and shear modulus were improved due to these additives by 64.45, 33.33, 29.51, 31.14, 30.14 and 27.58%, respectively. It was also observed that the presence of BHA and MgO nanoparticles enhanced the bioactivity, optical and electrical properties of the prepared samples. The results obtained are encouraging and the aim of this study has been successfully achieved.

Keywords: Poly (vinyl alcohol); Hybrid composites; Bioactivity; Hydroxyapatite; Mechanical properties; Optical properties; Bone repair applications

1. Introduction

The second most common surgical procedures in the United States that needs tissue transplantation is for bone abnormalities brought on by trauma, tumors, or age. Although autografting is the greatest option for treating bone defects, there are still some limitations to this technique, including the fact that bone tissue is frequently unavailable and necessitates additional surgery, which increases the patient's discomfort. As a result, it is still difficult for researchers in orthopedics to design novel synthetic bone replacements that have characteristics that are comparable to or even near to those of genuine bone [1]. One such potential alternative bone material is poly (vinyl alcohol; PVA), thanks to its outstanding properties such as innate lack of toxicity, lack of carcinogenicity, strong biocompatibility, and desirable physical features [2, 3]. However, PVA alone has drawbacks like poor cell attachment to tissues, bioinert nature and low mechanical capabilities. The PVA matrix will thus be able to get around these issues and perform better if an organic or inorganic additive is added to it [4].

*Corresponding author e-mail: dhamoda@ut.edu.sa & daliaabulyazied78@gmail.com.; (Dalia E. Abulyazied), rhakamnrc@gmail.com.; (Rasha A. Youness).
Received date 12 November 2023; revised date 30 December 2023; accepted date 07 January 2024
DOI: https://doi.org/10.21608/ejchem.2024.247968.8852

Hydroxyapatite (HA; $Ca_{10}(PO_4)_6(OH)_2$), a bioceramic, is present in considerable amounts in all vertebrate bone tissue. As a result, it may be applied in many biological contexts, such as middle ear implants and bone augmentation. Significantly, it exhibits enhanced characteristics like surface grain size, pore size, and wettability when synthesized at the nanoscale range [5]. Egg shells, seashells, animal bones, and corals have all been used extensively over the past 20 years in research on the utilization of biogenic structures and materials to create HA powders using various synthesis procedures. Not only does the production of HA powders utilizing biogenic materials require biogenic resources, but waste recovery also has economic and environmental advantages. Because of its physical similarities to human bone, HA produced from biogenic sources like animal bones may be less likely to be rejected by living tissues [6].

Magnesium oxide (MgO) nanoparticles have attracted a lot of attention in recent years due to their appealing properties, which include a high surface area to volume ratio, thermal and electrical insulation, a potent capacity to adsorb toxic gases and dye wastes, antimicrobial activity, nontoxicity, and biocompatibility [7]. Owing to these exceptional features, MgO nanoparticles have found extensive usage as a catalyst, ceramic material, thermal and electrical insulator, bactericide, material to handle hazardous liquid and gaseous wastes, multifunctional composites, and a refractory material [8, 9]. Additionally, materials containing Mg^{2+} ions were shown to be advantageous for bone regeneration techniques since this element accelerated the mending of bone defects [10]. It is also important to note that MgO is one of the magnesium compounds that the Food and Drug Administration (FDA) has approved as safe [11]. According to this, MgO nanoparticles are being thought of as one possibility to strengthen a variety of biopolymers [12].

Silica-based ceramics are another group of bioactive products, which exhibit better biodegradability in comparison to HA ceramics, promote apatite nucleation and enhance bone bonding in vivo [13]. In addition, silica-based materials encourage deposition of extracellular matrix, which facilitates cell adhesion and other cellular activities [14]. Silicon carbide (SiC) ceramic is one of the members of this group which is light in weight and has excellent mechanical and tribological properties [15]. It has been used in the manufacture of composite bone scaffolds, thanks to its outstanding properties including biocompatibility and lack of cytotoxicity [16].

As a result of the previously mentioned drawbacks of PVA that restricted its use in bone replacement applications, many researchers around the world have been interested in improving the mechanical properties and bioactivity of PVA through the addition of HA [17-19]. However, the mechanical properties of the resulting PVA/HA composites were not significantly improved as a result of the low mechanical properties of HA which also need to be improved. For this reason, this study is concerned with the improving the various properties that include mechanical, optical, electrical and biological properties not only for PVA or HA but also for PVA/HA composites by adding appropriate materials to obtain composites suitable for the purposes of bone tissue repair, which has not been studied by anyone in the literature according to the knowledge of the authors

2. Materials and methods

2.1. Production of biological hydroxyapatite (BHA) nanopowders

Bones from animals, specifically camels, were used to create BHA nanoparticles. Then were then divided into uniformly sized pieces, each measuring 5 cm, and left to soak for 2 h in a solution of acetone and ethyl alcohol. To get rid of stuck-on fats and other contaminants, they were then boiled for 3 h. Following a 3 h boil, the bones were calcined in an electrical furnace at 800 °C at a 5-degree-per-minute heating rate. The resultant BHA was then ground into a nanoscale-sized particles using a high-energy ball mill (HEBM) for 3 h at a ball-to-powder ratio (BPR) of 10:1 with a ball diameters = 10 mm and speed of 300 rpm. Notably, the milling cycle was limited to 30 min and was then halted for 30 min. The resulting BHA powders were examined by X-ray diffraction (XRD; Philips PW 1373) technique, Fourier transform infrared (FTIR; type Jasco-300E Japan) spectroscopy and high resolution transmission electron microscopy (HRTEM; JEOL JEM-2100 Japan, operated at accelerating voltage of 120 kV).

2.2. Preparation of PVA/BHA/MgO/SiC composites powders

As briefly mentioned in the preceding section, BHA nanoparticles have been created, whilst pure PVA, SiC, and MgO (99.5%, 99.99%, and 99.95% purity, respectively) have been purchased. Then, to

evaluate the purchased PVA, MgO, and SiC powders, the XRD technique, FTIR spectroscopy and HRTEM were once more applied. PVA, BHA, SiC, and MgO powders were mechanically blended according to their volume percentages displayed in Table 1.

Table 1
Scheme of the prepared composites referring to the sample code and its composition (vol.%)

Sample code	PVA	BHA	MgO	SiC
MS0	70	30	0	0
MS2.5	70	30	2.5	0.5
MS5	70	30	5	1
MS7.5	70	30	7.5	2
MS10	70	30	10	4

2.3. Hot–press molding

The circular sample was created by loading the material into a cylindrical mold and applying heat. The hot-press molding required 120 °C, 250 MPa, and 8 min, respectively, of temperature, pressure, and time. The plates were demolded and kept at temperature after cooling.

2.4. The characterization of the prepared PVA/BHA/MgO/SiC composites

Using the XRD method, the pre-existing phases in the composites sintered at 120 °C were examined. Field emission scanning electron microscopy-coupled with energy dispersive spectroscopy (FESEM-EDS; type Philips XL3000) were employed to examine the microstructure of the as-prepared samples.

2.5. The bioactivity behavior of the investigated samples

By immersing the samples in simulated body fluid (SBF) made in accordance with the instructions provided by Kokubo *et al*. [20] preserving the ratio of sample grains to volume of solution=0.01 g/ml [21], the in vitro bioactivity of the resulting composites was evaluated after 14 days by FESEM. The soaking samples were then put under SEM to look at the HA layer that had grown on their surfaces.

2.6. Different properties of the prepared samples

2.6.1. Physical properties

The relative density and apparent porosity of the prepared composites were determined using Archimedes' method [22, 23].

2.6.2. Mechanical properties

The manufactured specimens' microhardness was determined using a UNITED TRU-BLUE UNIVERSAL hardness tester in accordance with ASTM: B933-09, as stated in Refs. [24,25]. Importantly, indentations were measured for each data point for at least five samples. However, each specimen had its compressive strength assessed in accordance with ASTM E9. Furthermore, the longitudinal and shear ultrasonic wave velocities propagated in the samples were ascertained at room temperature using the pulse-echo technique and an ultrasound digital signal processing (DSP) system made by MATEC Model MBS8000. The values of Lame's constants (λ and μ) may be calculated using longitudinal (V^2_L) and shear (V^2_S) ultrasonic velocities in the manner described below [26,27]:

$$\lambda = \rho(V_L^2 - 2V_S^2) \quad \ldots\ldots\ldots\ldots\ldots\ldots (1)$$

$$\mu = \rho V_S^2 \quad \ldots\ldots\ldots\ldots\ldots\ldots (2)$$

The longitudinal modulus (*L*), shear modulus (*S*), shear Young's modulus (*Y)*, bulk modulus (*B*), and Poisson's ratio (*υ*) of the nanocomposites were calculated by the following equations [28,29]

$$L = \lambda + 2\mu \quad \ldots\ldots\ldots\ldots\ldots\ldots (3)$$

$$S = \mu \quad \ldots\ldots\ldots\ldots\ldots\ldots (4)$$

$$Y = \mu\frac{3\lambda+2\mu}{\lambda+\mu} \quad \ldots\ldots\ldots\ldots\ldots\ldots (5)$$

$$B = \lambda + \frac{2}{3}\mu \quad \ldots\ldots\ldots\ldots\ldots\ldots (6)$$

$$\upsilon = \frac{\lambda}{2(\lambda+\mu)} \quad \ldots\ldots\ldots\ldots\ldots\ldots (7)$$

where ρ is the measured density of glass samples, L is the longitudinal modulus, S is the shear modulus, Y is Young's modulus, B is the bulk modulus, and v is the Poisson's ratio.

2.6.3. Optical properties

With the help of a UV-Vis spectrophotometer of the JASCO570 design, the optical measurements of the tested substances were examined.

2.6.4. Electrical properties

The electrical conductivity (σ) of the sintered composites was measured at room temperature, using Keithley 616 system according to the formula [30]:

$$\sigma = \frac{h}{RA} \quad \text{..... (8)}$$

where R, h and A are the electrical resistance, the diameter of the specimen and the surface area of specimen, respectively.

3. Results and discussion

3.1. Characterization of the starting materials

The crystal structure of the starting materials, such as PVA, BHA, MgO, and SiC, was investigated using XRD equipment as shown in Fig. 1 (a-d), respectively. Analyzing the collected data and contrasting it with the ICCD file card would reveal the clarity of distinct BHA XRD peaks without the presence of any other XRD peaks. This result suggests that collagen and lipids, which are undesirable organic pollutants, were not present during BHA production. The characteristic XRD peaks of PVA, MgO and SiC were also significantly identified according to the standard XRD cards. The initial substances, PVA, BHA, MgO and SiC, may also be found to be in the nano–scale range based on the observed broadness in their diffraction peaks. One of the most important advantages of nanostructured biomaterial is their improved capacity to interact with proteins and bone-forming cells [31].

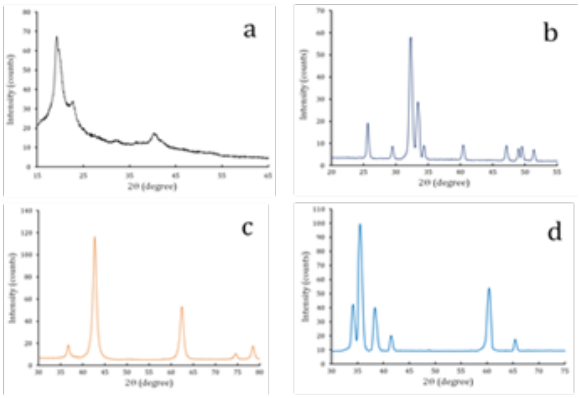

Fig. 1. XRD patterns of the starting materials, i.e. a) PVA, b) BHA, c) MgO, and d) SiC.

The ability to characterize the chemical composition and crystallinity of polymers using infrared spectroscopy has shown to be very helpful. When combined with other methods, it may provide more comprehensive details on the network structure and chemical functions of the materials [27]. To illustrate this, FTIR absorption spectra were captured and shown in Fig. 2 (a-d). It should be mentioned that the resulting bands' assignments were made with the aid of relevant research publications [32-34]. In Fig 2a, the primary characteristic bands of tension and bending vibration of the O–H, C–H, C–O, and C=O groups were present in the FTIR spectra recorded for PVA material. A stretching vibration of O–H was seen between 3200 and 3300 cm^{-1}. Methylene group stretching in both asymmetric and symmetric fashion was visible in bands at 2940 and 2990 cm^{-1}. The absorption band at 1720 cm^{-1} could be connected to the stretching vibration of the carbonyl C=O groups in the major chains of PVA. In addition, the existence of OH or CH bending vibrations may be the cause of the absorption band at 1660 cm^{-1}. Also, connected to the bending and wagging of CH_2 vibrations are the bands at 1440 and 1375 cm^{-1}. An absorption band at 1256 cm^{-1} results from CH wagging. In actuality, the detected band at 1142 cm^{-1} is typically considered to be an evaluation tool to look at the crystalline structure of PVA. The presence of the characteristic BHA bands at 1087, 1023, 960, 630, 600, 563, 470 and 430 cm^{-1} in Fig. 2b, which may be attributable to the different vibrational modes of PO_4^{3-} groups, shows how well BHA is produced. Moreover, there is a weak band at 1625 cm^{-1} that could be the cause of the OH^- vibrational mode in the HA molecule. In addition, the weak bands located near 870, 1480 and 1420 cm^{-1} can be assigned to the vibrations of carbonate (CO_3^{2-}) groups. In Fig. 2c, the stretching mode of the OH group, which was discovered as a result of H_2O adsorption on the MgO surface, may be the cause of the broad area between 3600 and 800 cm^{-1}. The Mg–O–Mg vibration modes of MgO can be linked to a prominent band seen at 760 cm^{-1}. The stretching and bending vibrations of Si–C are responsible for the absorption bands at ~1400 and 830-800 cm^{-1} that are seen in Fig. 2d, respectively.

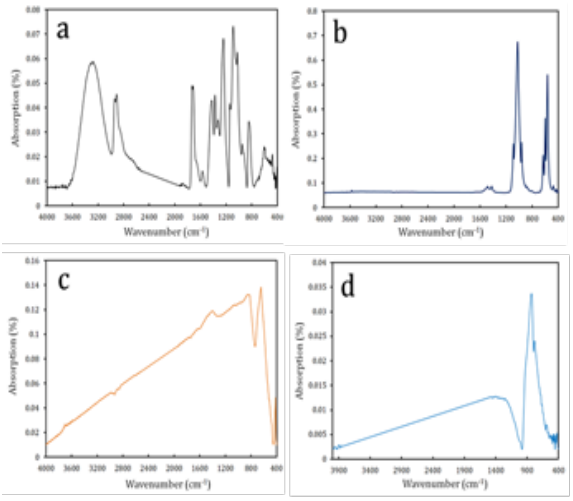

Fig. 2. FTIR absorption spectra of the starting materials, i.e. a) PVA, b) BHA, c) MgO and d) SiC.

Fig. 3 (a-d) displays the particle sizes of the used PVA, BHA, MgO, and SiC powders. Obviously, the pictures obtained in these figures show that the BHA, MgO, and SiC powders are made up of spherical nanoparticles and appear to be relatively agglomerated. Notably, the average particle sizes for PVA, BHA, MgO, and SiC are 1.21 µm, 71.9 nm, 45.5 nm and 39.2 nm, respectively.

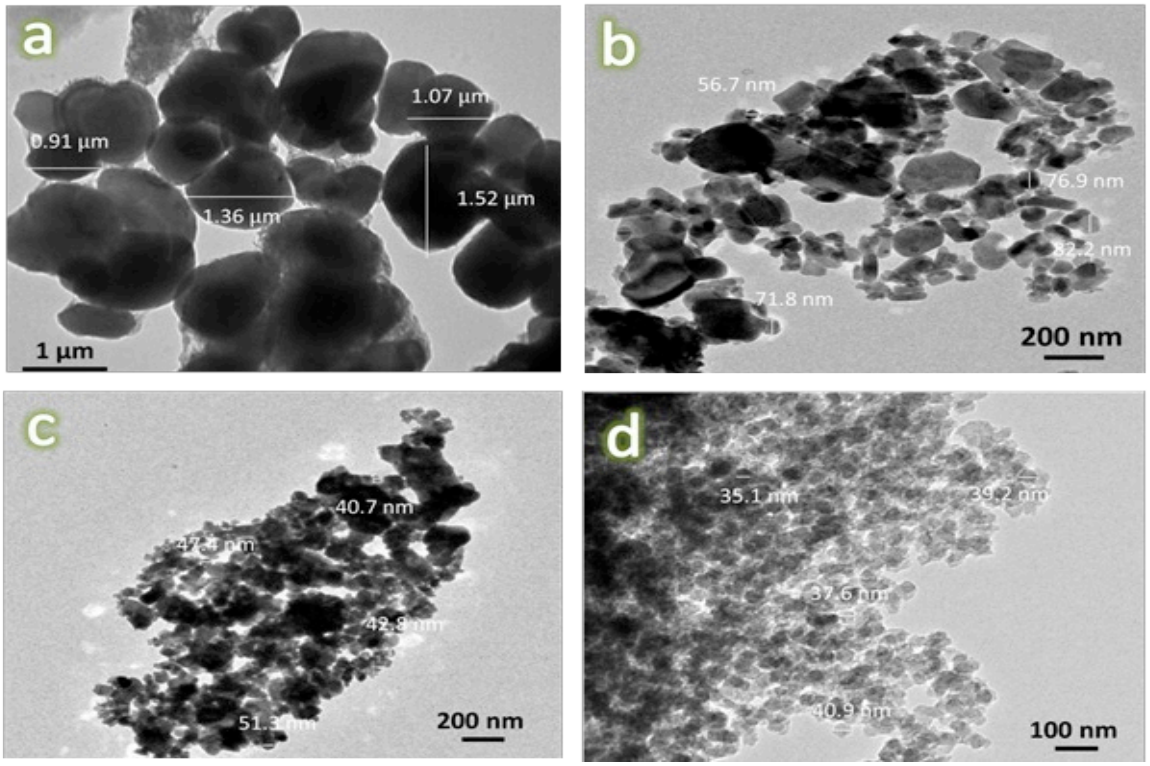

Fig. 3. HRTEM images of the starting materials used in the preparation of composites, i.e. a) PVA, b) BHA, c) MgO and d) SiC

3.2. Characterization of the sintered PVA/BHA/MgO/SiC composites

3.2.1. XRD analysis

The XRD pattern of each sample is displayed in Fig. 4. The following key observations are supported by this figure and can be summarized as follows:

a. It is clear to distinguish the typical PVA, BHA, MgO, and SiC XRD peaks considering that the intensity of the peaks belonging to PVA and BHA decreases noticeably with increases in MgO and SiC contents.

b. Other than the peaks for PVA, BHA, MgO and SiC, no other peaks could be seen on the X-ray diffractogram, proving that there were no contamination issues during the creation of the composites or the heating procedure and that the component phases of these composites did not interact.

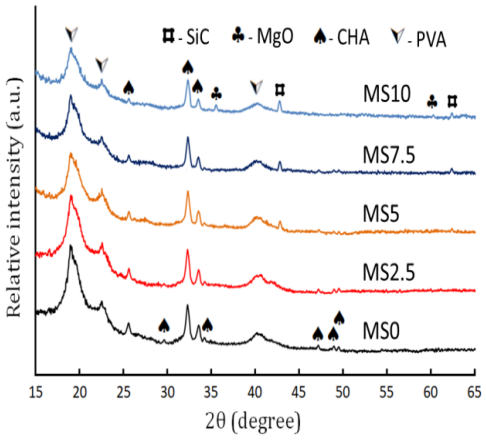

Fig. 4. XRD patterns of PVA/BHA/MgO/SiC of hot–pressed composites at 120 °C.

3.2.2. Investigation of the microstructure of the samples by FESEM

As shown in Figs. 5 (a-e) and 6 (a-e), the FESEM was used to examine the microstructure of all produced samples at two magnification powers; namely 6000 and 12000 X. Figure 5a demonstrates what a dense MS0 sample looks like with a uniform dispersion of small BHA nanoparticles. This observation was confirmed by analyzing the image obtained for the same sample at 12000 X magnification.

It should be noted that this conclusion is based on the presence of small holes present in the structure. Interestingly, although the reader expected that successive addition of MgO and SiC would significantly reduce the densification of the samples due to the large difference between the higher melting point (2852 and 2730 °C, respectively) compared to the melting point of PVA (200 °C) in addition to the low temperature used to prepare these composites, but Fig. 5 (b-e) shows that this prediction is not entirely correct because the decrease in densification of the samples was slightly. This amazing result can be better explained by relating these findings to those discussed in Section 3.1 which revealed that all the additives were very fine and located in the nanoscale range which further contributed to the pore closure. Good densification may be indicated by large grains, few pores, and firm contact between the grains.

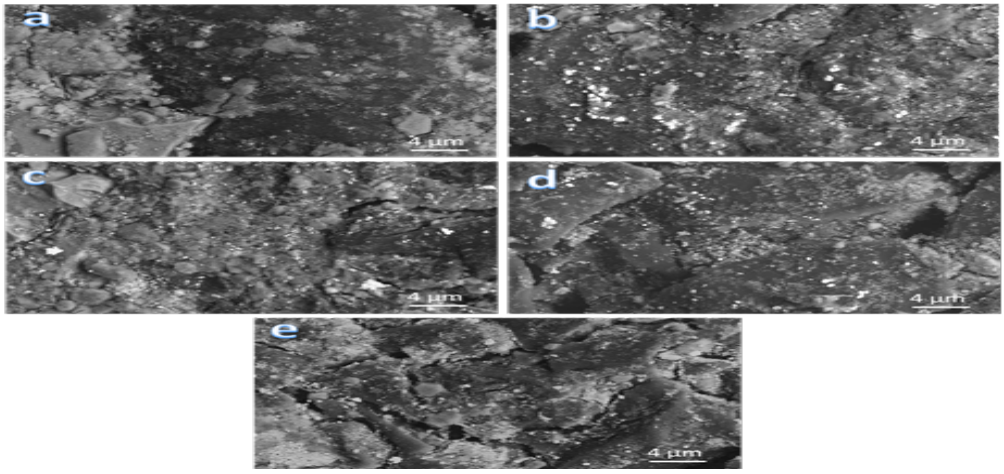

Fig. 5. FESEM micrographs of all prepared composites with a magnification of 6000 X

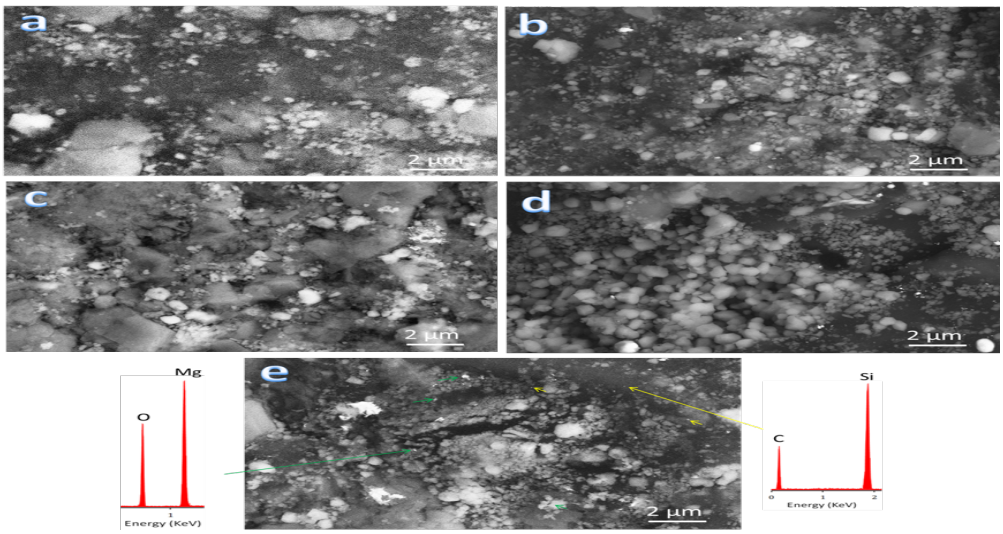

Fig. 6. FESEM micrographs of all hot–pressed samples with a magnification of 12000 X coupled to the EDS pattern of the MS10 sample to show the added chemical elements, i.e. MgO and SiC.

3.3. Bioactivity behavior of the investigated samples

In order for any biomaterial to stably bond with living bones when implanted in the human body, it is imperative that it generate a HA-like coating on its surface as a result of its interaction with the nearby physiological fluids [35]. In this context, the prepared MS0, MS5 and MS10 samples after incubation in SBF solution for 14 days were examined using the FESEM technique as shown in Fig. 7 (a-c), respectively. It is possible to see that Fig. 7 demonstrates the samples' bioactivity slightly increases and follows an escalating pattern in the following order: MS0<MS5<MS10. This conclusion is based on the observation of the gradual formation of the apatite layer covering the surfaces of the samples. It should be noted that since the percentage of HA is constant in all tested samples; this improvement in bioactivity may be related to the increase in MgO contents. Before discussing the role of MgO in enhancing the bioactivity of the samples, the mechanism for the ability of HA to form an apatite layer on its surface after soaking in SBF solution must first be explained.

Fig. 7. FESEM micrographs of a) MS0, b) MS5 and c) MS10 samples after soaking in SBF solution for 14 days

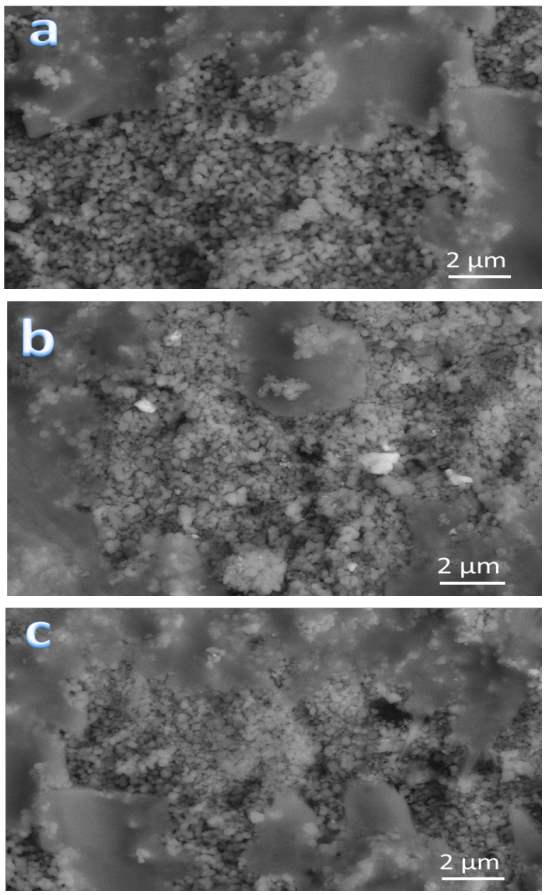

The bioactivity of HA can be explained by one of two mechanisms. First, is primarily based on the fact that it contains negative charges, phosphate $(PO_4)^{3-}$ ions that can interact with positive charged ones, calcium (Ca^{2+}) ions in the SBF solution, and amorphous calcium phosphate (Ca–P) layer formed on its surface. It combines with PO_4^{3-} ions in SBF to form calcium–deficient amorphous Ca–P layer, which then crystallizes into deposits that resemble bone on the surface of HA. Second, since it can release Ca^{2+} and PO_4^{3-} ions under physiological circumstances into the surrounding fluid and subsequently precipitate bone–like apatite on its surface, is strongly connected to the dissolving capabilities of HA. The second rationale is disregarded since the evaluated bioactivity was performed in vitro by soaking these samples in SBF solution [36]. According to what has been reported from the literature [37, 38], the role of MgO in enhancing the biologically active behavior of the tested samples can be attributed to its high ability to degrade into SBF according to the following equation:

$$MgO_{(s)} + H_2O_{(aq.)} \text{ …….. } Mg^{2+}_{(aq.)} + 2\ OH^-_{(aq.)} \text{ ……..…… (9)}$$

As a result, the dissolution of Mg^{2+} ions further improves the formation of the apatite layer which is important for bone bonding ability [39].

4.1. Different properties of the prepared samples

4.1.1. Physical properties

The relative density and apparent porosity of the prepared composites were measured and represented in Fig. 8 (a,b), respectively. It is clear that the relative density of the samples decreases with increasing vol.% of the ceramics used, i.e. MgO and SiC. On the contrary, the apparent porosity exhibited an opposite trend to the relative density which is considered to be normal. Fortunately, this increase in apparent porosity is slight and does not have a considerable impact on the mechanical properties of the samples as will be discussed in the next section. The measured values of the apparent porosity for MS0, MS2.5, MS5, MS7.5 and MS10 samples are 2.5, 3.1, 3.7, 5.3 and 7.3%. This finding has significant biological implications since, according to many scientists, porosity promotes implant osseointegeration and vascularization processes unless it negatively affects the mechanical properties of the implant material in the bone. Moreover, it must be emphasized that the produced composites' porosity values, which range from 5 to 13%, are quite equivalent to compact bone [40, 41]. These results are consistent with those discussed in Section 3.2.2.

Fig. 8. a) Relative density, and b) apparent porosity of the prepared samples

4.1.2. Mechanical properties

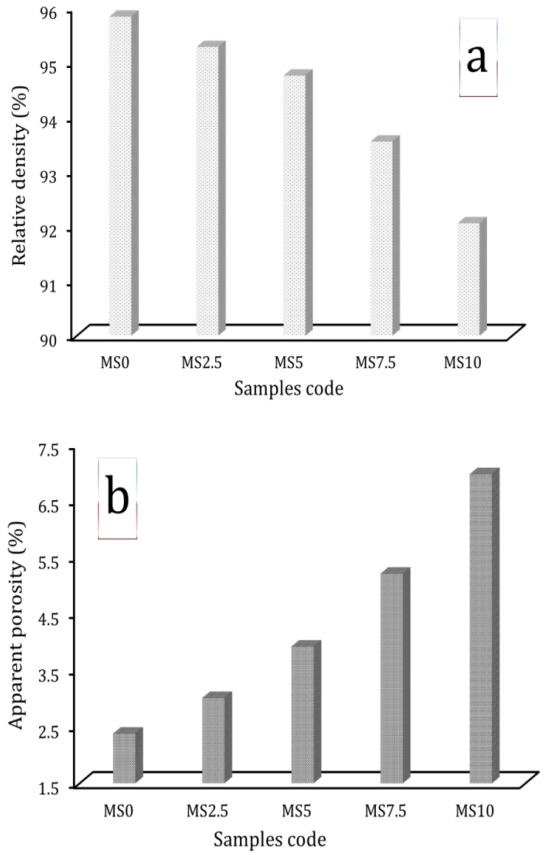

Microhardness, compressive strength, Young's modulus, longitudinal modulus, bulk modulus, shear modulus and Poisson's ratio of the prepared MS0, MS2.5, MS5, MS7.5, and MS10 samples were measured and depicted in Figs. 9 and 10. The obtained results demonstrated that MgO and SiC had a favorable impact on all mechanical properties of the hot-pressed samples. For instance, the MS10 sample significantly improved microhardness, compressive strength, Young's modulus, longitudinal modulus, bulk modulus, shear modulus, and Poisson's ratio by about 64.45, 33.33, 29.51, 31.14, 30.14, 27.58, and 8.60%, respectively.

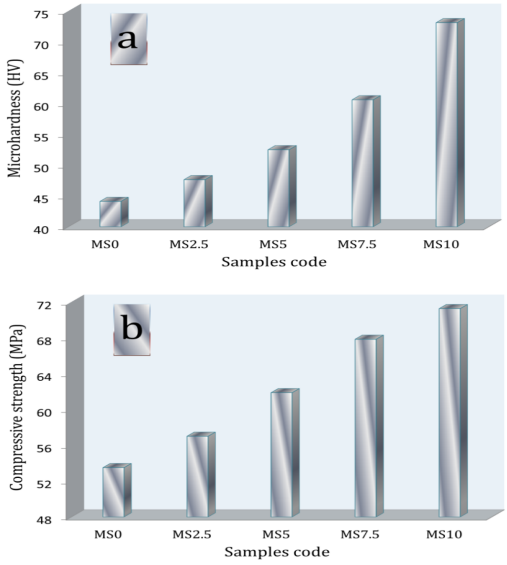

Fig. 9. a) Microhardness and b) compressive strength of hot–pressed PVA/BHA/MgO/SiC composites at 120 °C

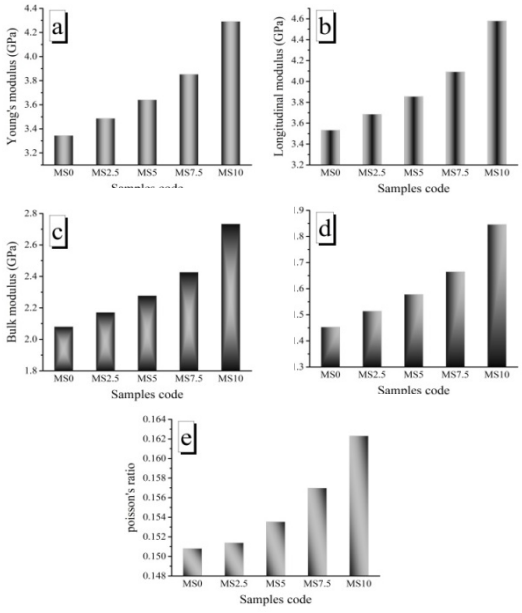

Fig. 10. a) Young's modulus, b) longitudinal modulus, c) bulk modulus, d) shear modulus, and e) Poisson's ratio for all hot–pressed samples.

4.1.3. Optical properties

In this work, UV/VIS/NIR spectrometer was used to measure the transmittance, absorbance, and reflectance of the prepared biocomposite materials. In general, electromagnetic radiation (ER) is known to interact

with the surface of any sample in a variety of ways, including absorption, transmission, reflectance, or scattering. In addition, the sample's externally reflected radiation may be specular or diffuse. The diffuse reflectance (DR) spectral method involves the reflection of incident light in all directions by irregular surfaces in various spectral ranges. The biocomposites' DR spectra with wavelength in the range from 180–1000 and 500–1000 nm are shown in Fig. 11 (a,b). It can be seen from this figure that the absorption edges at 239 nm shift toward a higher wavelength, i.e. 242 nm. Also, the intensity of this peak gradually increases with further loading of both SiC and MgO until the MS7.5 sample after which it showed a considerable decrease. According to these results, one can suggest that the biocomposite material can absorb the ER with wavelengths higher than those of HA and PVA [42, 43]. Therefore, the presence of both SiC and MgO nanoparticles can be homogeneously dispersed in the biocomposite material results in increase the total surface area and enhance the scattering efficiency of the DR up to the MS7.5 sample [44-46] while it decreased with MS10 sample due to a decrease occurs in the total surface area along with increasing the apparent porosity as seen before in FESEM images. The DR spectra show strong absorption band at wavelength lower than 400 nm. This finding can be attributed to the optical transitions that increase the optical band gap energy [47].

The DR spectra in the range within 500–1000 nm are depicted in Fig. 11b. It is reported that (R) increase from 53% in the case of the MS0 sample to 70% in the case of the MS10 sample at a wavelength of 500 nm by 24% and the scattering effect increased with increasing the content of SiC and MgO.

The optical band gap energy of biocomposites was determined using the Kubelka-Munk theory via DR [48-50].

$$F(R)=(1-R)^2/2R \quad \text{…….} \quad (10)$$

where R is the DR. The modified Tauc's eq. [51] used to calculate optical band gap energy.

$$F(R)_{h\nu}=A(h\nu - E_g)^n \quad \text{…….} \quad (11)$$

where α is the absorption coefficient, while hυ represents the energy of the incident photon and n=1/2 and 2 indicates by indirect and direct band gap transitions respectively. Figure 12 studied the relation between $[F(R)h\upsilon]^{0.5}$ with the photon energies (hυ), where the indirect energy gap $E_g^{indirect}$ was determined through the intercept value on the x–axis. The estimated $E_g^{indirect}$ values are listed in Table 2. It is increased from 3.88 to 5.12 eV with successive increase in the SiC and MgO contents up to the MS7.5 sample and after that it decreased to 4.51 eV in the MS10 sample. It is evident that the increment in optical band gap energy with increasing SiC and MgO content may be due to the decrease of the size of the formed agglomerates. The density and distribution of energy states change as a result of the quantum confinement effect, which occurs when SiC and MgO of a small enough size interlace with a PVA–HA matrix as seen in FESEM micrographs [52] while the decrement in its optical band energy gap with the MS10 sample is produced from the formation of the charge transfer complexes in the biocomposite material [42].

The refractive index (n) of biocomposite materials were calculated using the indirect energy gap $E_g^{indirect}$ gap [53]

$$\frac{n^2-1}{n^2+2}=1-\sqrt{\frac{E_g^{indirect}}{20}} \quad \text{…….} \quad (12)$$

The calculated refractive index is listed in Table 2. The refractive index values decreased from 2.17 to 1.97 with the increase of SiC and MgO up to the MS7.5 sample and increased to 2.07 in the MS10 specimen. According to these promising results, it can be concluded that the good reflectance characteristics obtained for the investigated biocomposites may be related to the healing of bone fractures [54].

Table 2
The indirect optical band gap energy and refractive index of all prepared samples

Sample code	$E_g^{indirect}$ (eV)	n
MS0	3.88	2.17
MS2.5	4.11	2.15
MS5	4.66	2.05
MS7.5	5.12	1.97
MS10	4.51	2.07

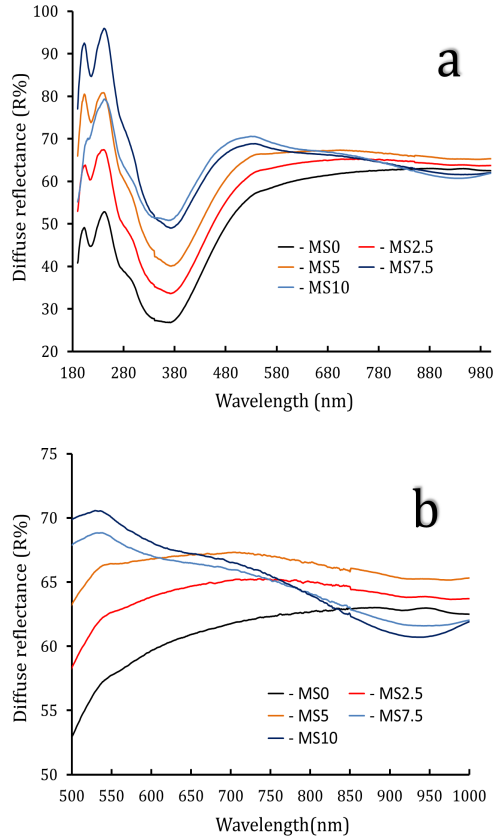

Fig. 11. UV–VIS–NIR diffuse reflectance spectra of the prepared biocomposite materials in the spectral range of a) 180–1000 and b) 500–1000 nm

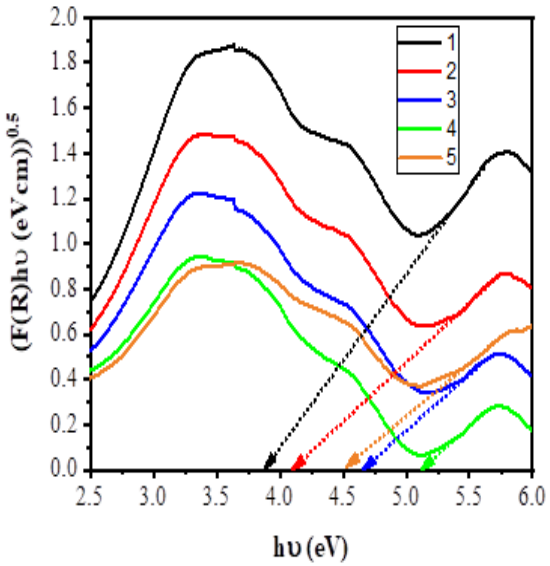

Fig. 12. Band gap energies of PVA/BHA/MgO/SiC composites

4.1.4. Electrical properties

Fig. 13 displays the DC conductivity values for MS0, MS2.5, MS5, MS7.5, and MS10 biocomposite samples at room temperature. Noteworthy, due to the accumulation of charges at the electrode contacts, which reduces the conductivity, the conductivity values are low at DC frequency [55]. In addition, the figure shows that the conductivity of the biocomposites increased to approximately 2-3 orders of magnitude compared to the MS0 sample. The reason for this significant increase in DC conductivity can be attributed to the increase of defect state density with increasing SiC and MgO content due to the formation of more defects and thus perturbation of the PVA/HA composite structure [56]. Additionally, as the concentration of SiC nanoparticles increases, the number of free charge carriers increases accordingly to generate a transport network within the composite materials and thus increase the conductivity [57].

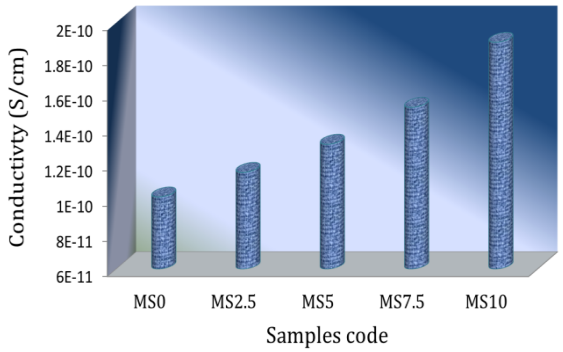

Fig. 13. The electrical conductivity of PVA/BHA/MgO/SiC composites

Conclusions

Extensive research work has been devoted to developing promising materials for use in bone replacement applications. In this context, researchers have focused part of their interest on the utilization of calcium phosphate (Ca-P) compounds, thanks to their attractive biological properties such as biocompatibility, bioactivity, degradability, etc. It should be noted that the Ca-P family can be divided into seven compounds such as hydroxyapatite, calcium deficient hydroxyapatite, dicalcium phosphate dihydrate, tricalcium phosphate, bi-, tri- and multi-phasic calcium phosphate, tetracalcium phosphate and octacalcium phosphate. Unfortunately, its mechanical

performance still needs to be improved. In response to this fact, a promising solution to confront this problem is the preparation of Ca-P/ceramic or Ca-P/polymer composites. At the end of this work, we would like to conclude that further work is needed to enhance the weak mechanical properties of Ca-P compounds to be suitable for biomedical applications.

Conflicts of interest

The manuscript was written through the contributions of all authors. All authors have approved the final version of the manuscript. The authors declare that they have no competing interests.

Formatting of funding sources

The authors extend their appreciation to the Deanship of Scientific Research at University of Tabuk for funding this work through Research No. (S-1443-0008).

Acknowledgement

The authors extend their appreciation to the Deanship of Scientific Research at the University of Tabuk for funding this work through Research No. (S-1443-0008)

References

1. B.D. Ratner, Annu. Rev. Biomed. Eng. 21 (2019) 171.
2. M. Jin, J. Shi, W. Zhu, H. Yao, Tissue Eng. Part B Rev. 27 (2021) 604.
3. D. Arcos, M.V. Regí, Acta Mater. 61 (2013) 890.
4. P. Parida, A. Behera, S.C. Mishra, Int. J. Adv. Appl. Sci. 1(3) (2012) 125.
5. K.M. Agarwal, P. Singh, U. Mohan, S. Mandal, D. Bhatia, Sensors Int. 1 (2020) 100055.
6. K. Tur, Turk J. Rheumatol. 24 (2009) 206.
7. A. Tathe, M. Ghodke, A.P. Nikalje, Int. J. Pharm. Pharm. Sci. 2 (4) (2010) 19.
8. H. Wang, Polymers 13 (2021) 3868
9. A.B.H. Yoruç, B.C. Şener, Biomaterials, a roadmap of biomedical engineers and milestones, Sadik Kara (Ed.), ISBN: 978-953-51-0609-8, InTech (2012)
10. R.A. Youness, M.A. Taha, M. Ibrahim, Mater. Chem. Phys. 257 (2021) 123264.
11. R.A. Youness, M.A. Taha, M.A. Ibrahim, J. Mol. Struct. 1150 (2017) 188.
12. R.A. Youness, M.A. Taha, M.A. Ibrahim, Mater. Chem. Phys. 239 (2020) 122011.
13. T.M. Hamdy, Egypt. J. Chem. 61 (4) (2018) 723.
14. D.E. Abulyazied, A.M. Alturki, R.A. Youness, H.M. Abomostafa, J. Inorg. Organomet. Polym. Mater. 31 (2021) 4077.
15. A.M. Alturki, D.E. Abulyazied, M.A. Taha, H.M. Abomostafa, R.A. Youness, J. Inorg. Organomet. Polym. Mater. 32 (2022) 169
16. J.P. Park, J.D. Bronzino (2003), Biomaterials: principles and applications. In: Kon Kim Y, Park JB, editors. Metallic Biomaterials. USA: CRC Press LLC. (2003), pp. 1-20.
17. A. B. Khoshaim, E. B. Moustafa, and R. A. Youness, Nanotechnol. Rev. 13 (2024) 1
18. R.A. Youness, M.A. Taha, H. Elhaes, Mater. Chem. Phys. 190 (2017) 209.
19. R.A. Youness, M.A. Taha, H. Elhaes, M. Ibrahim, J. Comput. Theor. Nanosci. 14 (2017) 2409.
20. A. Oryan, S. Alidadi, A. Moshiri, N. Maffulli, J. Orthop. Surg. Res. 9 (2014) 18.
21. R. Florencio-Silva, G.R. da Silva Sasso, E. Sasso-Cerri, M.J. Simoes, P.S. Cerri, Biomed Res. Int. 2015 (2015) 1.
22. A.M. Alturki, A.S. Alatawi, D.E. Abulyazied, H. M. Abomostafa, G. M. El komy, R. Alamlah, M.A. Taha, R.A. Youness, ECS. J. Solid. State. Sci. Technol.12 (2023) 083001
23. E.B. Moustafa, A. Aljabri, W.S. Abushanab, E. Ghandourah, M.A. Taha, A. B. Khoshaim, R. A.Youness, S. S. Mohamed, Sci. Rep.14 (2024) 2862
24. R.L. Elwan, A.A. El-Kheshen, R.A. Youness, M.A. Taha, Ceram. Int. 49(23) (2023) 37680
25. W.S. Abushanab, E.B. Moustafa, R.A. Youness, Appl. Phys. A. 129 (2023) 394
26. W.S. Abushanab, E.B. Moustafa, R.A. Youness, J. Non-Cryst. Solids 586 (2022) 121539
27. R.A. Youness, M.A. Taha, Sci. Rep.14 (2024) 2425
28. R.A. Youness, M.S. Amer, M.A. Taha, J. Inorg. Organomet. Polym. Mater.33 (2023) 4068
29. R.A. Youness, E. Al-Ashkar, M.A. Taha, Ceram. Int. 49(24) (2023) 40520
30. E.B. Moustafa, S.S. Abdel Aziz, M.A. Taha, A. Saber**,** Met. 13(5) (2023) 836
31. Y.J. Zhu, Chin. J. Chem. 35 (2017) 769.
32. M.N. Hassan, M.M. Mahmoud, A. Abd El-Fattah, S. Kandil, Ceram. Int. 42 (2016) 3725.
33. J. Jeong, J.H. Kim, J.H. Shim, N.S. Hwang, C.Y. Heo, Biomaterials Res. 23 (2019) 1.
34. J.S. Al-Sanabani, A.M. Madfa, F.A. Al-Sanabani, Int. J. Biomater. 2013 (2013) 876132.
35. S.K. Wong, Y.H. Wong, K.-Y. Chin, S. Ima-Nirwana, Polymers 31 (2021) 3075.
36. J. Lu, H. Yu, C. Chen, RSC Adv. 8 (2018) 2015.

37. H.H. Xu, P. Wang, L. Wang, C. Bao, Q. Chen, M.D. Weir, L.C. Chow, L. Zhao, X. Zhou, M.A. Reynolds, Bone Res. 5 (2017) 1.
38. D.A. Cardoso, J.A. Jansen, S.C.G. Leeuwenburgh, J. Biomed. Mater. Res. B 100 (2012) 2316.
39. M.P. Ginebra, T. Traykova, J.A. Planell, J. Control. Release 113 (2) (2006) 102.
40. A.A. Majhool, I. Zainol, C.N.A. Jaafar, A.H.A. Alsailawi, M.Z. Hassan, M. Mudhafar, A.A. Majhool, A. Asaad, J. Chem. Chem. Eng. 13 (2019) 112.
41. P. Dee, H.Y. You, S.-H. Teoh, H. Le Ferrand, J. Mech. Behav. Biomed. Mater. 112 (2020) 104078.
42. M. Tavoni, M. Dapporto, A. Tamipieri, S. Sprio, J. Compos. Sci. 5 (2021) 227.
43. F. Albee, H. Morrison, Ann Surg. 71 (1920) 32.
44. W. Habraken, P. Habibovic, M. Epple, M. Bohner, Mater. Today 19 (2) (2016) 69.
45. P.N. Kumta, C. Sfeir, D.H. Lee, D. Olton, D. Choi, Acta Biomater. 1 (2005) 65.
46. J.C. Elliott, Structure and chemistry of the apatites and other calcium orthophosphates, ed. by H.M. Hughes, (Amsterdam: Elsevier, 1994).
47. M. Canillas, P. Pena, A.H. de Aza, M.A. Rodríguez, Boletín de la Sociedad Española de Cerámica Y vidrio 56 (2017) 91.
48. N.A.S.M. Pu'ad, P. Koshy, H.Z. Abullah, M.I. Idris, T.C. Lee, Heliyon 5 (2019) 1.
49. A. Refaat, R.A. Youness, M.A. Taha, M. Ibrahim, J. Mol. Struct. 1147 (5) (2017) 148.
50. A. Nakahira, K. Nakata, C. Numako, H. Murata, K. Matsunaga, Mater. Sci. Appl. 2 (2011): 1194.
51. X. Li, Y. Deng, M. Wang, X. Chen, Y. Xiao, X. Zhang, J. Mater. Chem. B 6 (2018) 84.
52. R.A. Youness, M.S. Amer, M.A. Taha, Mater. Chem. Phys. 285 (2022) 126085
53. N. Eliaz, N. Metoki, Materials 10 (4) (2017) 1.
54. H.H.K. Xu, P. Wang, L. Wang, C. Bao, Q. Chen, M.D. Weir, L.C. Chow, L. Zhao, X. Zhou, M.A. Reynolds, Bone Res. 5 (2017) 1.
55. T. Albrektsson, C. Johansson, Eur Spine J 10 (2001) S96.
56. S.V. Dorozhkin, Biomaterials 31 (2010) 1465.
57. W.A. Elkhateeb, S.S.M. Morsi, M.E. Hassan, M.A. Taha, E.F. Ahmed, G.M. Zaghlol, Plant Arch. 20 (2020) 857